



Influence of the calcination procedure on the thermoelectric properties of calcium cobaltite $\text{Ca}_3\text{Co}_4\text{O}_9$

Sophie Bresch¹ · Björn Mieller¹ · Christian Selleng² · Thomas Stöcker³ · Ralf Moos³ · Torsten Rabe¹

Received: 12 April 2017 / Accepted: 19 February 2018 / Published online: 27 February 2018
© Springer Science+Business Media, LLC, part of Springer Nature 2018

Abstract

Calcium cobaltite is one of the most promising oxide p-type thermoelectric materials. The solid-state reaction (or calcination, respectively), which is well known for large-scale powder synthesis of functional materials, can also be used for the synthesis of thermoelectric oxides. There are various calcination routines in literature for $\text{Ca}_3\text{Co}_4\text{O}_9$ powder synthesis, but no systematic study has been done on the influence of calcination procedure on thermoelectric properties. Therefore, the influence of calcination conditions on the Seebeck coefficient and the electrical conductivity was studied by modifying calcination temperature, dwell time, particle size of raw materials and number of calcination cycles. This study shows that elevated temperatures, longer dwell times, or repeated calcinations during powder synthesis do not improve but deteriorate the thermoelectric properties of calcium cobaltite. Diffusion during calcination leads to idiomorphic grain growth, which lowers the driving force for sintering of the calcined powder. A lower driving force for sintering reduces the densification. The electrical conductivity increases linearly with densification. The calcination procedure barely influences the Seebeck coefficient. The calcination procedure has no influence on the phase formation of the sintered specimens.

Keywords Thermoelectric oxides · Calcination · Solid-state-synthesis · Power factor

1 Introduction

Thermoelectric materials can directly transform a temperature difference dT into a voltage U due to the Seebeck effect [1], defined by:

$$S = \frac{U}{dT} \quad (1)$$

Materials with a high Seebeck coefficient S , high electrical conductivity and low thermal conductivity can be used in thermoelectric generators for the recovery of heat, which is particularly interesting considering the limited primary energy resources [2]. Although the efficiency of thermoelectric

generators is by far smaller than the Carnot efficiency [1], they are used in remote applications because of their high reliability due to no moving parts. Cost-effective thermoelectric generators can improve the efficiency of primary power generators like power plants by converting a part of the waste heat into electrical power [2].

Conventional thermoelectric materials like tellurides and skutterudites have good thermoelectric properties, but are limited to lower temperatures ranges (up to 300 °C) as they melt or decompose at higher temperatures. In addition, their raw materials are toxic, rare and expensive. These conventional thermoelectric materials are also sensitive to oxidation [3].

An interesting alternative are oxide thermoelectric materials. Their thermoelectric performance is not as high as of the non-oxide materials, but they are less toxic, their raw materials are cheaper, and often more abundant. Additionally, they are stable at higher temperature in oxidizing atmosphere. By decreasing the production costs of oxide thermoelectric generators while maintaining or increasing their performance, these oxide generators could become practically relevant, especially for high temperature applications [2].

Two important measures are the power factor, PF , and the figure of merit, ZT , describing the electronic properties with respect to energy conversion. Material with a high PF require

✉ Sophie Bresch
sophie.bresch@bam.de

¹ Division Advanced Technical Ceramics, Bundesanstalt für Materialforschung und –prüfung (BAM), 12203 Berlin, Germany

² Division Building Materials, Bundesanstalt für Materialforschung und –prüfung (BAM), 12203 Berlin, Germany

³ Department of Functional Materials, University of Bayreuth, 95447 Bayreuth, Germany

a high Seebeck coefficient, S , and a good electrical conductivity, σ .

$$PF = S^2 \cdot \sigma \quad (2)$$

For a high figure of merit, ZT , a low thermal conductivity κ is necessary. ZT increases with the temperature, T , if all other material parameters are constant.

$$ZT = \frac{PF}{\kappa} T = \frac{S^2 \cdot \sigma}{\kappa} T \quad (3)$$

Today, doped SrTiO₃ [4, 5] and ZnO [6–8] show the best performance for n-type thermoelectrics at elevated temperatures. As high-temperature p-type materials, recent studies on delafossites like CuFeO₂ indicate good thermoelectric properties [9–11]. However cobaltites currently exhibit the highest ZT values among oxide p-type thermoelectrics [12–17]. One of the most promising material is calcium cobaltite Ca₃Co₄O₉ [2, 3, 15–18]. Ca₃Co₄O₉ has a layered crystal structure of alternating CoO₂ and Ca₂CoO₂ [19] and is stable in air up to 926 °C. At higher temperatures, it decomposes into Ca₃Co₂O₆ and CoO [19, 20]. Undoped, pressure-less sintered calcium cobaltite reaches Seebeck coefficients between 120 μ V/K and 135 μ V/K at room temperature [21–26] and 190 μ V/K to 220 μ V/K at temperatures between 600 °C and 800 °C [23–26]. The electrical conductivity varies between 1500 S/m and 9000 S/m at room temperature [21–26] and between 2500 S/m and 6500 S/m at 600 °C to 800 °C [23–27], respectively. The thermal conductivity amounts to 1 W/mK [28] to 6 W/mK [22]. Altogether, the power factor of undoped Ca₃Co₄O₉ reaches values between 28 μ W/K² m and 90 μ W/K² m at room temperature [23–26] and between 60 μ W/K² m and 200 μ W/K² m at 600 °C to 800 °C [23–26]. The figure of merit amounts to approximately 0.008 at 25 °C [21, 22, 28] and 0.09 at 600 °C [27, 28].

The two main synthesis routes for Ca₃Co₄O₉ are soft chemistry [16, 24, 29–31] and solid-state reaction [15, 21, 23, 25, 32–34], the latter is historically also known as mixed-oxide route. During a thermal process, known as calcination, the final phases are formed. The soft chemistry synthesis, such as co-precipitation of oxalates [29], polymer-solution synthesis [24] or Pecchini method [16, 24], result in Ca₃Co₄O₉ nanoparticles. The high surface area of such small particles increases the driving force for sintering and thus leads to a higher density and increases the electrical conductivity as shown by Sotelo et al. [24]. Soft chemistry synthesis causes higher powder synthesis costs than the mixed-oxide route, due to the expensive raw materials and the associated calcination step [35].

The solid-state reaction is cost-effective and easily scalable by using a rotary kiln and is therefore widely used as powder synthesis method for various functional materials like BaTiO₃ or PZT in industry [36]. Within

literature, a wide range of calcination procedures is used to synthesize Ca₃Co₄O₉. Stoichiometric amounts of the raw material (CaCO₃ and mainly Co₃O₄) were mixed with a planetary ball mill [15, 21, 23, 25, 32–34]. The calcination temperature varied between 750 °C [23] and 900 °C [21, 22, 25, 28, 32, 34]. The dwell time was at least 12 h [21, 23, 32] but mostly between 20 h [15] and 24 h [21, 22, 25, 28, 34]. Most authors repeated the calcination with an intermediate grinding step [15, 21–23, 27, 32]. Park et al. compacted the powder into pellets before calcination and used a pure oxygen atmosphere instead of air [34].

There are only a few studies examining the influence of the calcination procedure on the properties of Ca₃Co₄O₉. Smaczyński et al. [37] examined the influence of the temperature on the phase formation and showed that no Ca₃Co₄O₉ was formed for temperatures below 750 °C, whereas Ca₃Co₂O₆ was already present at 800 °C. The latter result is not in good accordance with the phase diagram [19, 20] and other studies as mentioned above [21, 22, 25, 28, 32, 34]. Thermoelectric properties were not tested. In a study by Yu et al. [38], the powder was calcined at 800 °C and 900 °C, respectively. They found Ca₃Co₄O₉ at 800 °C and Ca₉Co₁₂O₂₈ at 900 °C. The powder produced at 900 °C had a 1.5 times higher electrical conductivity. The influence on the Seebeck coefficient was not measured. Delorme et al. [39] reached a 30% higher electrical conductivity by using nano CaO (<100 nm) as raw material instead of powder with a grain size of 10–20 μ m. An influence on the Seebeck coefficient was not observed. Presečnik et al. [40] showed that longer milling times of the raw material mixture improved the electrical conductivity by a factor of 1.6.

In summary, the calcination procedure varies within the different studies. To the authors' knowledge, a systematic research of the solid-state powder synthesis procedure for Ca₃Co₄O₉ considering the thermoelectric properties has not yet been published.

As a high temperature process, the powder synthesis consumes a lot of energy. To produce cost-effective thermoelectric generators, a good knowledge of the powder synthesis is indispensable. In this study, the influence of the calcination procedure on the thermoelectric properties of Ca₃Co₄O₉ is analyzed using the design of experiment method (DoE).

2 Experimentals

2.1 Design of experiments

Statistical design of experiments allows getting a maximum of information from a minimum number of experiments. Therefore, several parameters p are examined at the same time. With a full factorial design, all effects of the parameter

and all interactions of the parameter can be analyzed. The number of experimental points n is given by

$$n = L^p \quad (4)$$

with the parameter levels L . The experimental points are randomized to minimize the effect of disturbances on certain parameters [41].

The main synthesis parameter (particle size of raw material, calcination temperature, and calcination dwell time) were examined with a 2^3 statistical design of experiments. The applied experimental framework is shown in Table 1. The mean particle size was varied between 1.6 μm and 2.3 μm (for particle size distribution see Fig. 1), the calcination temperature was varied between 800 $^\circ\text{C}$ and 900 $^\circ\text{C}$, and the dwell time between 6 h and 9 h. The number of calcination cycles was set to 2. Supplementary to the statistical design of experiments, the influence of the calcination cycles was investigated with additional experimental points (No 9–12). Therefore, the number of calcination cycles was varied between zero and three (0, 1, 2 3) and the other synthesis parameter were set to a constant level (mean particle size of raw materials: 2 μm , calcination temperature: 850 $^\circ\text{C}$, and dwell time: 9 h). The effects of the different parameters within the statistical design of experiments on the target values (linear shrinkage, sinter density, particle size after calcination, Seebeck coefficient and electrical conductivity) were analyzed with the statistics package Minitab 17 (Minitab Inc., State College, Pennsylvania, USA).

2.2 Material preparation

Stoichiometric amounts of calcium carbonate (99%, low-alkali, Riedel-de Haën, Seelze, Germany) and cobalt (II, III) oxide (99.97+ %, ChemPUR, Karlsruhe, Germany) were attrition milled (rotation speed: 800 min^{-1}) in ethanol with zirconia balls ($d=2.5$ mm). The ethanol was

evaporated in a rotary evaporator (Rotavapor R-124, Büchi, Essen, Germany). The milling time was varied to reach different particle size distributions (see Table 1 and Fig. 1). The powder mixtures were calcined in alumina sintering boats in air (for temperature and dwell time levels see Table 1), and afterwards dry-milled in a planetary ball mill (Pulverisette, Fritsch, Idar-Oberstein, Germany) with agate grinding bowls for 15 min with a rotation speed of 215 min^{-1} . 1.5 wt% pressing additives (Zusoplast 9002 and Optapix AC 95, Zschimmer & Schwarz, Lahnstein, Germany) were added to a water-based suspension of the powder. After drying, the mixture was grinded to obtain flakes of powder with pressing additives finer than 200 μm . Five test bars (50 mm \times 5 mm \times 5 mm) of each composition were uniaxially cold pressed (30 MPa) and sintered at 900 $^\circ\text{C}$ for 24 h in air.

2.3 Characterization

After each milling step, the particle size distributions of the powders were analyzed with a laser diffraction system (Mastersizer 2000, Malvern Instruments, Malvern, United Kingdom). Before and after sintering, the dimensions of the test bars were measured with a micrometer gauge (height h , width w) and with a caliper gauge (length l). The specimens were weighed (weight m) with an analytical balance with a resolution of 0.1 mg before and after sintering.

The linear shrinkage dl/l_0 was calculated according to:

$$dl/l_0 = \frac{l_0 - l_1}{l_0} \quad (5)$$

with length before sintering l_0 and length after sintering l_1 . The apparent density (geometric density) ρ was calculated according to formula (6).

Table 1 Experimental framework with parameter settings of the varied calcination conditions

	Experimental point No.	D50 raw materials	Dwell time	Calcination temperature	Calcination cycles
Design of Experiments	1	2.3 μm	6 h	800 $^\circ\text{C}$	2
	2	1.6 μm	6 h	800 $^\circ\text{C}$	2
	3	2.3 μm	12 h	800 $^\circ\text{C}$	2
	4	1.6 μm	12 h	800 $^\circ\text{C}$	2
	5	2.3 μm	6 h	900 $^\circ\text{C}$	2
	6	1.6 μm	6 h	900 $^\circ\text{C}$	2
	7	2.3 μm	12 h	900 $^\circ\text{C}$	2
	8	1.6 μm	12 h	900 $^\circ\text{C}$	2
Calcination cycles	9	2 μm	–	–	0
	10	2 μm	9 h	850 $^\circ\text{C}$	1
	11	2 μm	9 h	850 $^\circ\text{C}$	2
	12	2 μm	9 h	850 $^\circ\text{C}$	3

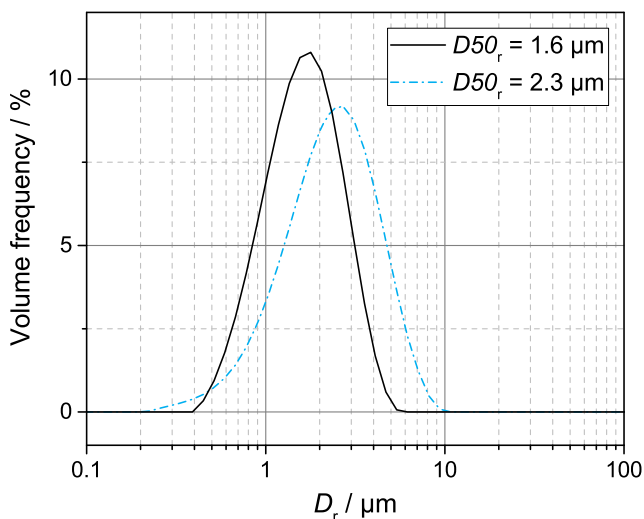


Fig. 1 Particle size distribution of the raw material mixture after attrition milling measured with a laser diffraction system. The milling time was set to 15 min for a $D50_r = 2.3 \mu\text{m}$ and to 45 min for a $D50_r = 1.6 \mu\text{m}$

$$\rho = \frac{m}{l \cdot w \cdot h} \quad (6)$$

The mass loss of the test bars was determined according to formula (7) with weight before sintering m_0 and weight after sintering m_1 :

$$dm/m_0 = \frac{m_0 - m_1}{m_0} \cdot 100\% \quad (7)$$

The microstructures of the samples were examined on polished as well as on fractured surfaces using a scanning electron microscope (Gemini Supra 40, ZEISS, Jena, Germany) fitted with an energy-dispersive X-ray spectrometer (EDX). The grain morphology was analyzed with the imaging software PixelFerber (Berlin, Germany) by measuring the maximum feret diameters of at least 100 grains. The phase compositions of the sintered samples were studied with X-ray powder diffraction (XRD) by means of synchrotron radiation because of its excellent intensity and very short required measurement time. These measurements were performed at the microfocus beamline μSpot (BEISSY II, Helmholtz Centre Berlin for Materials and Energy, Germany) in transmission geometry. The XRD patterns were collected for 30 s, with a wavelength of 1.0039 \AA by a Si (111) double-crystal monochromator and recorded using a two-dimensional MarMosaic CCD X-ray detector. An algorithm from the FIT2D software was used to process the obtained scattering images and to convert them into diagrams of scattered intensities versus scattering vector q ($q = 4\pi \sin\theta / \lambda$). For a direct comparison to the results by XRD with Cu radiation, the q -values were converted to the diffraction angle 2θ (Cu-K α 1).

The electrical resistance R of the test bars at room temperature was measured with a 4-probe-method using a digital multimeter (3458A, Hewlett Packard, Santa Rosa, USA).

The measurement was repeated two-times for top surface and bottom surface of the specimen. According to eq. (8) the electrical conductivity σ was calculated using the resistance R , the dimension of the test bars (h , w), and the distance of the two inner probes d .

$$\sigma = \frac{d}{R \cdot h \cdot w} \quad (8)$$

To determine the Seebeck coefficient S at room temperature, a laboratory setup was used. The two ends of the test bars were heated or cooled with Peltier elements to establish temperature differences from 1.5 K to 3 K between the two test probes. Two thermocouples type K with a distance of approximately 2 cm were used as test probes to measure both temperature difference ΔT and Seebeck voltage U . The Seebeck voltage was measured between the two chromel wires of the thermocouples. The Seebeck coefficients of the specimens $S_{\text{Test bar}}$ were calculated according to eq. (9), with $S_{\text{Chromel}} = 22.4 \mu\text{V/K}$ [42].

$$S_{\text{Test bar}} = \frac{U}{\Delta T} + S_{\text{Chromel}} \quad (9)$$

A measurement system analysis type-2 was performed to evaluate the repeatability and the reproducibility of the measurement setup for the Seebeck coefficient. The standard deviation of the total gage repeatability and reproducibility is 0.6%. A validation of the data was conducted with a laboratory setup of the Department of Functional Materials in Bayreuth, Germany. Data showed a systematic difference with the factor of 1.1.

3 Results

All powder synthesis conditions led to the formation of $\text{Ca}_3\text{Co}_4\text{O}_9$ after sintering. Figure 2 shows as an example the influence of the calcination cycles on the powder XRD pattern of sintered test bars. The XRD pattern of sintered test bars from uncalcined powder (experimental point No. 9) and powder that was calcined one time (No. 10), or three times (No. 12) at $850 \text{ }^\circ\text{C}$, for 9 h with a mean particle size of the raw materials $D50 \approx 2 \mu\text{m}$ are presented, respectively. The powder diffractograms of all samples were similar, with a main phase identified as $\text{Ca}_3\text{Co}_4\text{O}_9$ [43] and a minor phase identified as Co_3O_4 (PDF 01–080-1534). The peak intensity of the minor phase was so low that no quantitative XRD analysis was possible. None of the investigated powder synthesis parameters had a significant influence on the phase composition after sintering. The decomposition product $\text{Ca}_3\text{Co}_2\text{O}_6$ (PDF 00–051-0311) was not found.

Figure 3 shows the micrographs of fractured surfaces from sintered test bars. For a better illustration of the influence of

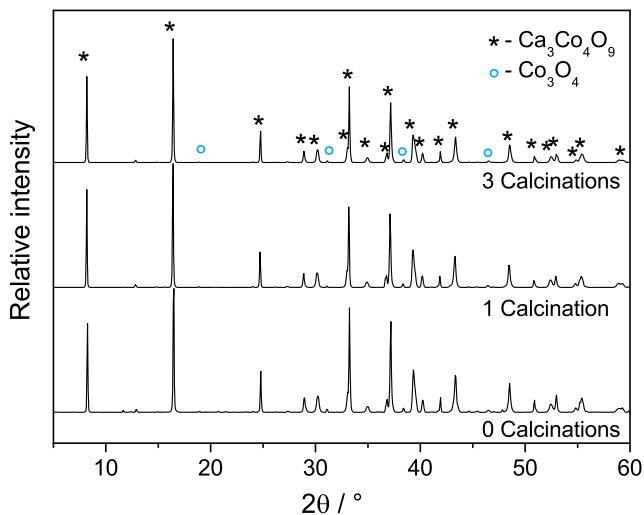
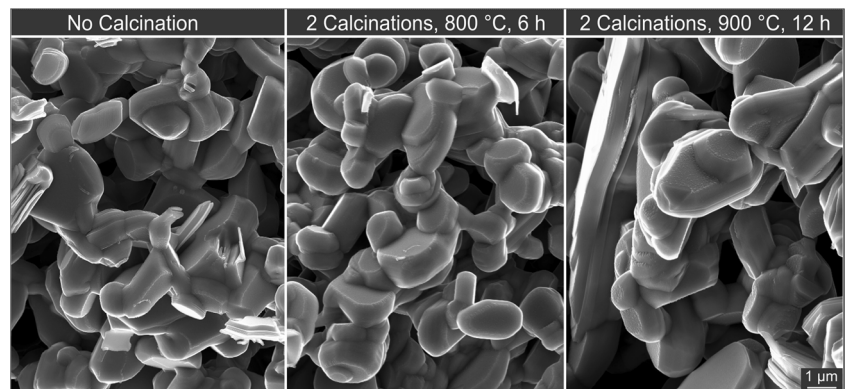


Fig. 2 Example for XRD pattern ($\lambda = \text{Cu-K}\alpha 1$) of sintered test bars produced by different calcination routes ($T_{\text{calc}} = 850\text{ }^\circ\text{C}$, $t_{\text{dwell}} = 9\text{ h}$, $D50_r \approx 2\text{ }\mu\text{m}$, experimental points No. 9, 10, 12)

the calcination procedure on the microstructure, the three examples with the largest differences in the microstructure were chosen. The examples are a reaction sintered test bar (no calcination, experimental point No. 9), a sintered test bar (No. 2) from powder calcined at low temperatures ($800\text{ }^\circ\text{C}$) for a short dwell time (6 h) and a sintered test bar (No. 7) from powder calcined at high temperatures ($900\text{ }^\circ\text{C}$) for a long dwell time (12 h). As shown in Fig. 3, the grains in the sintered test bars have a mica-like morphology and sinter-necks have formed between the grains. The grains are randomly orientated. The grains from calcined powder are more rounded than the ones in the reaction sintered test bars. Reaction sintered test bars and test bars from calcined powder at low temperatures for a short dwell time ($800\text{ }^\circ\text{C}$, 6 h) have a similar mean grain size (ferret diameter) after sintering of about $1.9\text{ }\mu\text{m}$. Higher calcination temperature and longer dwell time ($900\text{ }^\circ\text{C}$, 12 h) increase the mean grain size of the microstructure to $2.7\text{ }\mu\text{m}$, the anisotropy of the grains is more pronounced.

Figure 4(a) shows a micrograph of a polished surface with some pores, light-grey areas (marked with an oval), and a dark-grey matrix. For better illustration, a micrograph with

Fig. 3 SEM micrograph of fractured surface of sintered test bars from uncalcined powder ($D50_r \approx 2\text{ }\mu\text{m}$, No. 9), from powder calcined two times at $800\text{ }^\circ\text{C}$ for 6 h ($D50_r \approx 1.6\text{ }\mu\text{m}$, No. 2), and from powder calcined two times at $900\text{ }^\circ\text{C}$ for 12 h ($D50_r \approx 2.3\text{ }\mu\text{m}$, No. 7)



an above-average number of light-grey areas was chosen. The corresponding EDX-mapping for Co and Ca is shown in Fig. 4(b, c), respectively. The dark-grey matrix of the microstructure contains both Ca and Co (according to quantitative analysis of EDX spectrum of point 1: approximately 25 mol% Co, 18 mol% Ca and 56 mol% O) The light-grey phase contains Co but indicate no Ca (according to quantitative analysis of EDX spectrum of point 2: approximately 40 mol% Co and 60 mol% O). Such compositional inhomogeneities are found for all tested synthesis conditions. The area fractions of these inhomogeneities do not change regarding for example calcination cycles or calcination temperature.

The specimens produced from uncalcined powder had a mass loss of 18.9%, whereas all other experimental points lead to a mass loss of about 1.1%. Based on the data (physical and thermoelectric properties) gained from the experimental points No. 1–8 of the statistical design of experiments shown in Table 1, the fitted means and standard errors were calculated for the two parameter levels of mean particle size of raw materials ($D50_r$), calcination temperature (T) and calcination dwell time (t), respectively. The corresponding graphs (main effect plots) for the particle size of the calcined powder ($D50_c$), linear shrinkage (dl/l_0), electrical conductivity (σ) and Seebeck coefficient (S) are shown in the first three columns of Fig. 5. The last column of Fig. 5 shows the results of the additional experimental points No. 9–12 shown in Table 1 meaning the influence of the calcinations cycles on particle size of the calcined powder ($D50_c$), linear shrinkage (dl/l_0), electrical conductivity (σ) and Seebeck coefficient (S), respectively. In summary the influence of the calcination conditions on the physical and thermoelectrical properties at room temperature are shown in Fig. 5. By varying the calcination procedure within the experimental framework, the electrical conductivity can be increased by the factor of 2.1, the linear shrinkage by the factor of 12.6, and the particle size of the calcined powder by the factor of 2.2. The Seebeck coefficient remained almost constant. The power factor can be increased by the factor of 2.1 and reaches a maximum value of $30\text{ }\mu\text{W}/\text{mK}^2$. Assuming a thermal conductivity between $1\text{ W}/\text{mK}$ [28] and $6\text{ W}/\text{mK}$ [22], the figure of merit ZT amounts to 0.002 or

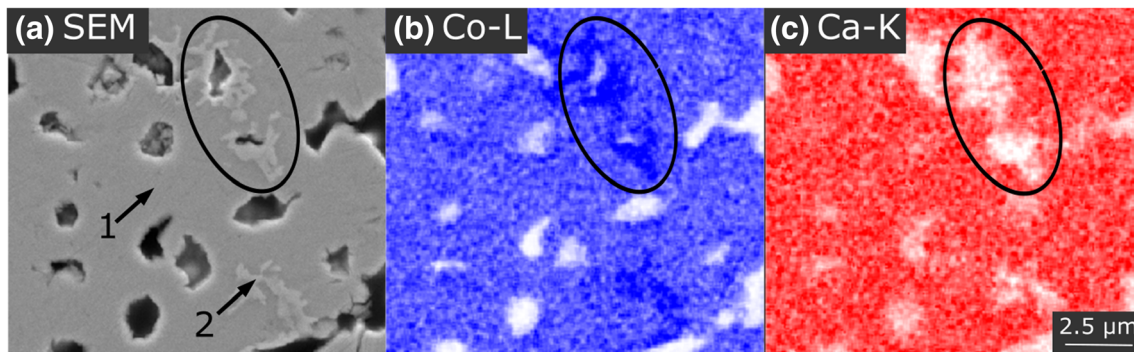


Fig. 4 (a) SEM micrograph of polished surface with SE detector. Areas in light grey are marked with an oval. Areas for EDX point analysis are marked with an arrow. (b) Corresponding netto peak areas of Co-L- α

X-ray-line (EDX-mapping) in blue and (c) corresponding netto peak areas of Ca-K- α X-ray-line in red with an acceleration voltage of 10 kV

0.009 at room temperature, respectively. As shown in the first column of Fig. 5, a smaller particle size of the raw materials ($D50_r$) decreases the particle size of the calcined powder ($D50_c$) by the factor of 0.9. Simultaneously, it increases the linear shrinkage by the factor of 2.2, the electrical conductivity by the factor of 1.1, as well as the power factor by the factor of 1.1. A higher calcination temperature (second column of Fig. 5) leads to a grain coarsening by the factor of 1.25 and

decreases the linear shrinkage by the factor of 0.5. Shorter dwell times (third column of Fig. 5) increase the Seebeck coefficient slightly by the factor of 1.01. As shown in the last column of Fig. 5, the number of calcination cycles had the biggest influence on the thermoelectric and physical properties. In particular, the difference between calcined and uncalcined powder is remarkable. The electrical conductivity is almost 2 times higher for the bars produced from uncalcined

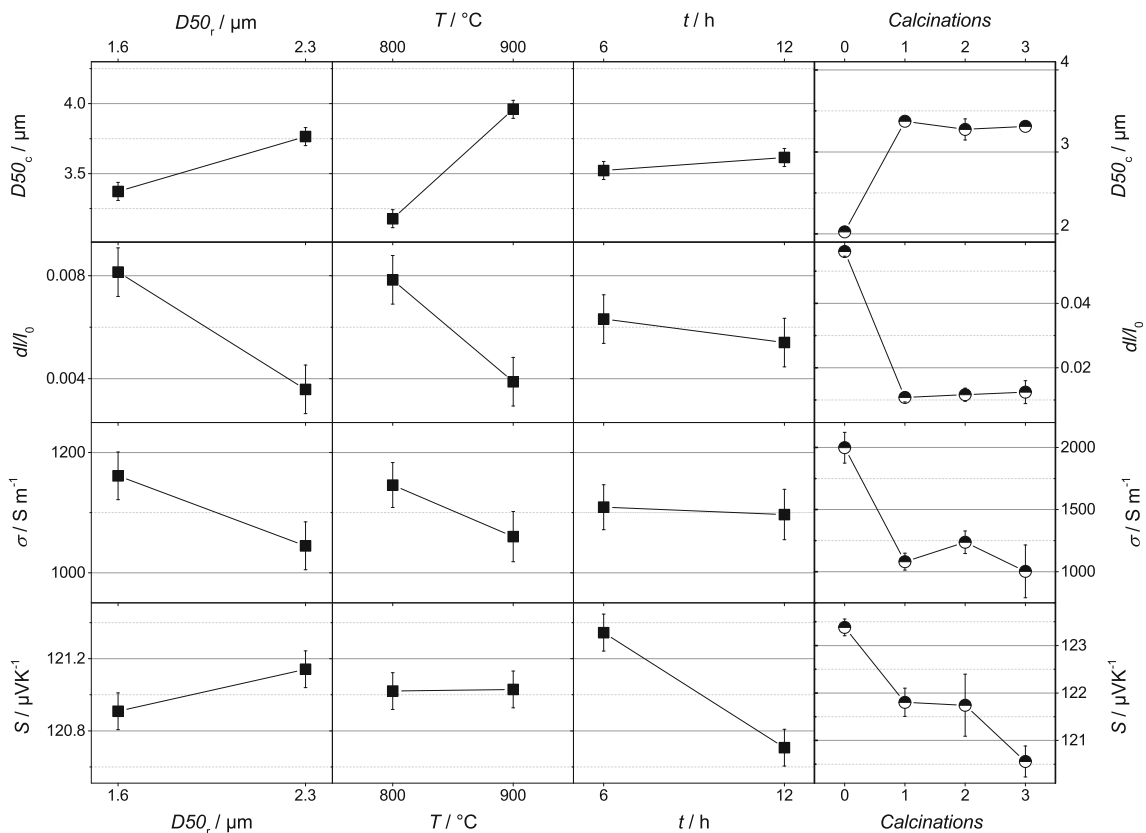


Fig. 5 Physical and thermoelectrical properties at room temperature as a function of the varied calcination parameters described in Table 1. This means Seebeck coefficient (S), electrical conductivity (σ), linear shrinkage (dl/l_0) and particle size of calcined powder ($D50_c$) as function of particle size raw materials ($D50_r$), calcination temperature (T), dwell time (t) and calcination cycles. The first three columns ($D50_r$,

T , t) show the fitted means and corresponding standard errors from the statistical design of experiments (No. 1–8). The last column ($Calcinations$) shows the means and standard deviation from the additional experimental points (No. 9–12). Please pay attention to the different ordinate scales on the right hand side ($Calcinations$)

powder than for those produced from powder, which was calcined three times; the Seebeck coefficient remains almost constant, the power factor doubles, and the linear shrinkage increases by the factor of 4.5. Test bars produced from uncalcined powder have the smallest grain size ($D_{50} \approx 2.0 \mu\text{m}$), highest shrinkage ($dl/l_0 = 0.06$), highest electrical conductivity ($\sigma = 2000 \text{ S/m}$), highest Seebeck coefficient ($S = 123 \mu\text{V/K}$), and therefore also the highest power factor ($\text{PF} = 30 \mu\text{W/mK}^2$). Within the experimental framework shown in Fig. 5 and Table 1 no significant influence (proofed by analysis of variance, ANOVA, with a level of significance, $\alpha = 0.1$) was found for the following parameters: particle size of raw materials on Seebeck coefficient; calcination temperature on electrical conductivity, Seebeck coefficient, and power factor; dwell time on particle size of calcined powder, linear shrinkage, electrical conductivity and power factor. No significant interactions (proofed by analysis of variance, ANOVA, with a level of significance, $\alpha = 0.1$) were found within the statistical design of experiments.

4 Discussion

Considering the XRD-pattern, the EDX-mapping, and EDX-analysis, the dark-grey matrix in Fig. 4 consist of $\text{Ca}_3\text{Co}_4\text{O}_9$, whereas the light-grey phase is Co_3O_4 . We assume that Co_3O_4 are remains of unreacted starting material. For all synthesis conditions, we find minor inhomogeneities in the XRD pattern and EDX-mapping probably caused by an incomplete solid-state reaction. According to phase and microstructural analysis, a more energy intensive powder synthesis like repeated calcination cycles, or higher calcination temperatures does not increase the phase content of $\text{Ca}_3\text{Co}_4\text{O}_9$ remarkably. In contrast to Smaczyński et al. [37], no $\text{Ca}_3\text{Co}_2\text{O}_6$ was found, even at calcination temperatures of $900 \text{ }^\circ\text{C}$.

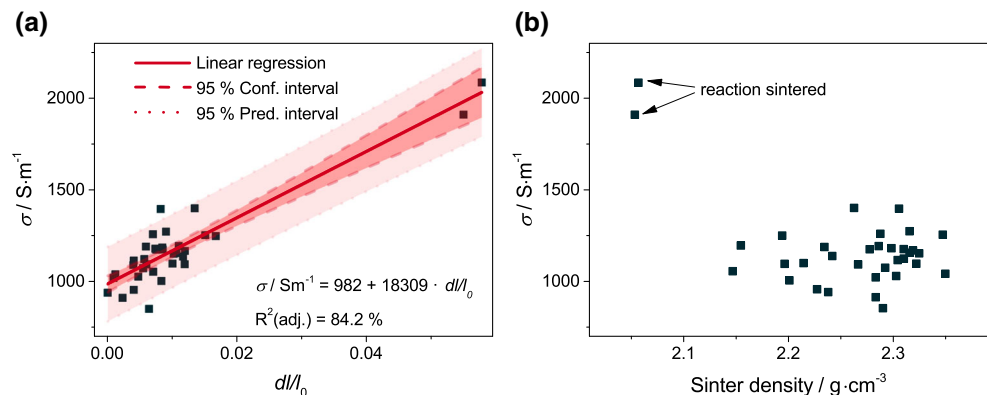
The calcination procedure has only a minor effect on the Seebeck coefficient in comparison to the other investigated properties. The Seebeck coefficient is an integral material property and is mainly dependent on the carrier concentration

and carrier mobility in the low-resistive volume of the $\text{Ca}_3\text{Co}_4\text{O}_9$ grains [44]. They may change in the equilibrium with the oxygen partial pressure of the calcination atmosphere [11] but this has not been investigated here.

The electrical conductivity of the specimen rises if the raw material grain size gets smaller, if the calcination temperature gets lower, and if the material is less often calcined. The linear shrinkage shows a similar dependency to these parameters. Figure 6(a) shows an increase of the electrical conductivity with increasing shrinkage of the specimens. A linear regression to the data shows a good adjusted coefficient of determination ($R^2(\text{adj.}) = 84.2\%$), especially with respect to the standard deviation of the underlying conductivity measurements. In contrast, the electrical conductivity is not dependent on the bulk sinter density of the specimens within the experimental framework ($R^2(\text{adj.}) = 0\%$, for linear correlation) as shown in Fig. 6(b). In theory with increasing sinter density, the density of the charge carriers per volume increases [45]. Therefore, a higher sinter density should lead to a higher electrical conductivity. Calcium cobaltite is known for very low shrinkage rates [46] and low relative densities after sintering [27, 46, 47]. Within the experimental framework, the sinter density varied only in the range of 8% of the absolute value, whereas the electrical conductivity varied in the range of 50% of the absolute value. Combined with the high standard deviation of the electrical conductivity measurements (repeatability amounts to about 10% of the absolute value), the variations in sinter density are probably not high enough to show an increase in electrical conductivity with increasing sinter density as published in literature [45].

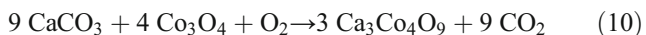
Regarding the given experimental framework with a generally low level of densification and only slight density variations between the different experimental points, it can be concluded that the electrical conductivity is mainly depending on the connection between the particles. Specimens with a higher shrinkage are in a more advanced sintering state. An advanced

Fig. 6 (a) Electrical conductivity as a function of linear shrinkage with linear regression, confidence interval and prediction interval. (b) Electrical conductivity as a function of sinter density



sintering state is characterized by stronger rearrangement of the particles and larger contact areas. Due to the increased intergranular contact area, charge transport between grains is enhanced, resulting in higher electrical conductivity.

A schematic diagram of the influence of the calcination procedure on the driving force for sintering is shown in Fig. 7. The calcination process leads to reaction (10) by reducing the chemical potential of the CaCO_3 and Co_3O_4 powder mixture.

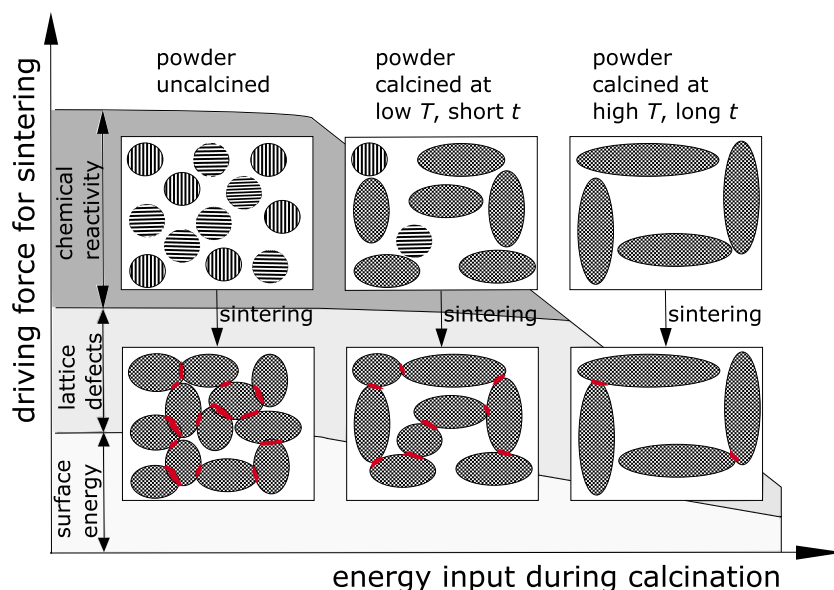


Calcium cobaltite is known to form anisotropic mica-like crystals due to its layered crystal structure [43]. The calcination process triggers surface diffusion, which promotes idiomorphic grain growth (Figs. 3 and 7) by minimizing lattice defects and surface energy [48]. The diffusion process during calcination minimizes the driving force for sintering of the powder. Therefore, the shrinkage during sintering is decreased and fewer intergranular contact areas (marked as thick interfaces in Fig. 7) are formed. This reduces the electrical conductivity of the specimens. Although it is common practice to calcine at high temperatures for long dwell times [15, 21, 23, 25, 32–34], for a high PF such a high energy input during calcination is not favorable.

Comparing the reaction sintered test bars with the test bars produced from calcined powder, they have the highest shrinkage (see Fig. 5), the highest mass loss, the lowest sinter density (see Fig. 6(b)) and the highest electrical conductivity (see Figs. 5 and 6(a)). Having the highest electrical conductivity and at the same time the lowest density seems like a contradiction as the charge

carrier density should decrease with decreasing density. But the improved properties of sintered test bars from uncalcined powder can be attributed to the different sinter mechanism in comparison to calcined powder. Solid state sintering is the densification mechanism for test bars from calcined $\text{Ca}_3\text{Co}_4\text{O}_9$ powder. Due to the decomposition temperature of $\text{Ca}_3\text{Co}_4\text{O}_9$, the sinter temperature is limited to 926 °C. As known, this leads to very low shrinkage (below 5%) even for long dwell times (over 24 h) [46]. By using calcium carbonate and cobalt (II, III) oxide as raw materials for the production of test bars, reaction sintering under the formation of $\text{Ca}_3\text{Co}_4\text{O}_9$ occurs. CaCO_3 dissociates into CaO and CO at about 825 °C and Co_3O_4 into CoO and O_2 at about 900 °C [49]. Therefore, the Hedvall-effect of enhanced chemical reactivity around phase changes [50] supports the sintering at 900 °C. This goes along with higher mass loss and higher shrinkage rates, as the reduction of the chemical potential during $\text{Ca}_3\text{Co}_4\text{O}_9$ formation is effective as additional driving force for sintering [51]. The higher mass loss during reaction sintering (19% for uncalcined powder to 1% for calcined powder) leads to the lower sinter density compared to the test bars from calcined powder. At the same time the higher driving force for sintering increases the linear shrinkage and the intergranular contact areas. The larger intergranular contact area would increase the charge carrier transport although the sinter density is lower. In conclusion, with respect to the generally low level of densification at 900 °C, reaction sintering of non-calcined raw materials results in a more interconnected $\text{Ca}_3\text{Co}_4\text{O}_9$ microstructure than sintering of any calcined $\text{Ca}_3\text{Co}_4\text{O}_9$ powder, thus giving higher electrical conductivity and better thermoelectric performance.

Fig. 7 Influence of calcination procedure on driving force for sintering. Raw materials with stripes pattern, calcium cobaltite with chess pattern. Contact areas are marked in red



5 Summary

The influence of the calcination temperature, dwell time, calcination cycles and particle size of raw materials on the properties of $\text{Ca}_3\text{Co}_4\text{O}_9$ were successfully studied with a statistical design of experiments (DoE). The calcination procedure had no influence on the phase content of the sintered test bars. Sintered test bars from uncalcined powder had the highest thermoelectric properties ($\sigma \approx 2000 \text{ S/m}$, $S \approx 123 \text{ } \mu\text{V/K}$, $PF \approx 30 \text{ } \mu\text{W/mK}^2$ at $22 \text{ } ^\circ\text{C}$) within the examined parameter settings. Repeated calcinations, higher calcination temperatures, and longer dwell times result in decreased thermoelectric properties and shrinkage. The electrical conductivity is correlated linearly with the shrinkage, but no correlation was found between density and thermoelectric properties. The calcination procedure barely influenced the Seebeck coefficient. In summary, a higher linear shrinkage leads to a higher power factor. Therefore, a powder with large driving force for sintering should be used to reach high shrinkage. Thermal processes that cause grain growth without densification should not be used during powder synthesis. $\text{Ca}_3\text{Co}_4\text{O}_9$ can efficiently be synthesized by direct reactive sintering of raw materials, without any additional calcination procedure. Thereby, the energy demand for the powder synthesis is reduced, which is an important step towards a cost-effective production of oxide thermoelectric generators.

Acknowledgements The authors are very grateful to the BAM colleagues S. Benemann for the SEM micrographs, F. Emmerling for XRD-analyses, T. Marcus for the electrical conductivity setup, F. Lindemann for analyzing the particle size distribution and W. Guether for the helpful advice.

References

- G.S. Nolas, J. Sharp, J. Goldsmid, *Thermoelectrics - Basic Principles and New Materials Developments* (Springer-Verlag, Berlin, 2001), pp. 2–3
- J.W. Fergus, Oxide materials for high temperature thermoelectric energy conversion. *J. Eur. Ceram. Soc.* **32**(3), 525–540 (2012)
- K. Koumoto, R. Funahashi, E. Guilmeau, Y. Miyazaki, A. Weidenkaff, Y. Wang, C. Wan, X.D. Zhou, Thermoelectric ceramics for energy harvesting. *J. Am. Ceram. Soc.* **96**(1), 1–23 (2013)
- S. Ohta, T. Nomura, H. Ohta, K. Koumoto, High-temperature carrier transport and thermoelectric properties of heavily La- or Nb-doped SrTiO_3 single crystals. *J. Appl. Phys.* **97**(3), 034106 (2005)
- R. Moos, A. Gnudi, K.H. Hardtl, Thermopower of $\text{Sr}_{1-x}\text{La}_x\text{TiO}_3$ ceramics. *J. Appl. Phys.* **78**(8), 5042–5047 (1995)
- K. Park, K.Y. Ko, W.S. Seo, W.S. Cho, J.G. Kim, J.Y. Kim, High-temperature thermoelectric properties of polycrystalline $\text{Zn}_{1-x-y}\text{Al}_x\text{Ti}_y\text{O}$ ceramics. *J. Eur. Ceram. Soc.* **27**(2–3), 813–817 (2007)
- M. Ohtaki, K. Araki, K. Yamamoto, High thermoelectric performance of dually doped ZnO ceramics. *J. Electron. Mater.* **38**(7), 1234–1238 (2009)
- H. Yamaguchi, Y. Chonan, M. Oda, T. Komiyama, T. Aoyama, S. Sugiyama, Thermoelectric properties of ZnO ceramics co-doped with Al and transition metals. *J. Electron. Mater.* **40**(5), 723–727 (2011)
- C. Ruttanapun, B. Boonchom, M. Thongkam, S. Kongtaweelert, C. Thanachayanont, A. Wichainchai, Electrical and optical properties of p-type $\text{CuFe}_{1-x}\text{Sn}_x\text{O}_2$ ($x = 0.03, 0.05$) delafossite-oxide. *J. Appl. Phys.* **113**(2), 023103 (2013)
- T. Nozaki, K. Hayashi, T. Kajitani, Thermoelectric properties of delafossite-type oxide $\text{CuFe}_{1-x}\text{Ni}_x\text{O}$ ($0 < x < 0.05$). *J. Chem. Eng. Jpn* **40**(13), 1205–1209 (2007)
- T. Stockner, J. Exner, M. Schubert, M. Streibl, R. Moos, Influence of oxygen partial pressure during processing on the thermoelectric properties of aerosol-deposited CuFeO_2 . *Materials* **9**(4), 227 (2016)
- P.H. Tsai, T. Norby, T.T. Tan, R. Donelson, Z.D. Chen, S. Li, Correlation of oxygen vacancy concentration and thermoelectric properties in $\text{Na}_{0.73}\text{CoO}_{2-\delta}$. *Appl. Phys. Lett.* **96**(14), 141905 (2010)
- F. Kenjiro, M. Tadashi, N. Kazuo, High-temperature thermoelectric properties of $\text{Na}_x\text{CoO}_{2-\delta}$ single crystals. *Jpn. J. Appl. Phys.* **40**(7R), 4644 (2001)
- K. Park, K.Y. Ko, J.G. Kim, W.S. Cho, Microstructure and high-temperature thermoelectric properties of CuO and NiO co-substituted NaCo_2O_4 . *Mater. Sci. Eng. B* **129**(1–3), 200–206 (2006)
- G. Xu, R. Funahashi, M. Shikano, I. Matsubara, Y. Zhou, Thermoelectric properties of the Bi- and Na-substituted $\text{Ca}_3\text{Co}_4\text{O}_9$ system. *Appl. Phys. Lett.* **80**(20), 3760 (2002)
- H. Su, Y. Jiang, X. Lan, X. Liu, H. Zhong, D. Yu, $\text{Ca}_{3-x}\text{Bi}_x\text{Co}_4\text{O}_9$ and $\text{Ca}_{1-y}\text{Sm}_y\text{MnO}_3$ thermoelectric materials and their power-generation devices. *Phys. Status Solidi* **208**(1), 147–155 (2011)
- Y. Liu, Y. Lin, L. Jiang, C.-W. Nan, Z. Shen, Thermoelectric properties of Bi^{3+} substituted co-based misfit-layered oxides. *J. Electroceram.* **21**(1), 748–751 (2008)
- F. Ryoji, M. Ichiro, I. Hiroshi, T. Tsunehiro, M. Uichiro, S. Satoshi, An oxide single crystal with high thermoelectric performance in air. *Jpn. J. Appl. Phys.* **39**(11B), L1127 (2000)
- E. Woermann, A. Muan, Phase equilibria in the system CaO-cobalt oxide in air. *J. Inorg. Nucl. Chem.* **32**(5), 1455–1459 (1970)
- D. Sedmidubsky, V. Jakeš, O. Jankovsky, J. Leitner, Z. Sofer, J. Hejtmanek, Phase equilibria in ca-co-o system. *J. Solid State Chem.* **194**, 199–205 (2012)
- Y. Huang, B. Zhao, S. Lin, R. Ang, Y. Sun, M.A. White, Enhanced thermoelectric performance induced by Cr doping at ca-sites in $\text{Ca}_3\text{Co}_4\text{O}_9$ system. *J. Am. Ceram. Soc.* **97**(11), 3589–3596 (2014)
- Y. Huang, B. Zhao, R. Ang, S. Lin, W. Song, Y. Sun, Structure, magnetic and transport properties in $\text{Ca}_3\text{Co}_{4-x}\text{Sb}_x\text{O}_9$ ceramics. *J. Alloys Compd.* **574**, 233–239 (2013)
- G. Constantinescu, S. Rasekh, M.A. Torres, J.C. Diez, M.A. Madre, A. Sotelo, Effect of Sr substitution for ca on the $\text{Ca}_3\text{Co}_4\text{O}_9$ thermoelectric properties. *J. Alloys Compd.* **577**, 511–515 (2013)
- A. Sotelo, G. Constantinescu, S. Rasekh, M.A. Torres, J.C. Diez, M.A. Madre, Improvement of the thermoelectric properties of $\text{Ca}_3\text{Co}_4\text{O}_9$ using soft chemistry synthetic methods. *J. Eur. Ceram. Soc.* **32**(10), 2415–2422 (2012)
- D. Kenfaui, D. Chateigner, M. Gomina, J.G. Noudem, Anisotropy of the mechanical and thermoelectric properties of hot-pressed single-layer and multilayer thick $\text{Ca}_3\text{Co}_4\text{O}_9$ ceramics. *Int. J. Appl. Ceram. Technol.* **8**(1), 214–226 (2011)
- J.C. Diez, M.A. Torres, S. Rasekh, G. Constantinescu, M.A. Madre, A. Sotelo, Enhancement of $\text{Ca}_3\text{Co}_4\text{O}_9$ thermoelectric properties by Cr for co substitution. *Ceram. Int.* **39**(6), 6051–6056 (2013)
- T. Schulz, J. Topfer, Thermoelectric properties of $\text{Ca}_3\text{Co}_4\text{O}_9$ ceramics prepared by an alternative pressure-less sintering/annealing method. *J. Alloys Compd.* **659**, 122–126 (2016)
- D. Kenfaui, B. Lenoir, D. Chateigner, B. Ouladdiaf, M. Gomina, J.G. Noudem, Development of multilayer textured $\text{Ca}_3\text{Co}_4\text{O}_9$ materials for thermoelectric generators: Influence of the anisotropy on

- the transport properties. *J. Eur. Ceram. Soc.* **32**(10), 2405–2414 (2012)
29. F. Delorme, C.F. Martin, P. Marudhachalam, G. Guzman, D.O. Ovono, O. Fraboulet, Synthesis of thermoelectric $\text{Ca}_3\text{Co}_4\text{O}_9$ ceramics with high ZT values from a $\text{Co}^{\text{II}}\text{Co}^{\text{III}}$ -layered double hydroxide precursor. *Mater. Res. Bull.* **47**(11), 3287–3291 (2012)
 30. M. Sopicka-Lizer, P. Smaczyński, K. Kozłowska, E. Bobrowska-Grzesik, J. Plewa, H. Altenburg, Preparation and characterization of calcium cobaltite for thermoelectric application. *J. Eur. Ceram. Soc.* **25**(12), 1997–2001 (2005)
 31. R. Funahashi, M. Mikami, S. Urata, M. Kitawaki, T. Kouuchi, K. Mizuno, High-throughput screening of thermoelectric oxides and power generation modules consisting of oxide unicouples. *Meas. Sci. Technol.* **16**(1), 70–80 (2005)
 32. J.G. Noudem, S. Lemonnier, M. Prevel, E.S. Reddy, E. Guilmeau, C. Goupil, Thermoelectric ceramics for generators. *J. Eur. Ceram. Soc.* **28**(1), 41–48 (2008)
 33. R. Funahashi, S. Urata, Fabrication and application of an oxide thermoelectric system. *Int. J. Appl. Ceram. Technol.* **4**(4), 297–307 (2007)
 34. J.W. Park, D.H. Kwak, S.H. Yoon, S.C. Choi, Thermoelectric properties of highly oriented $\text{Ca}_{2.7}\text{Bi}_{0.3}\text{Co}_4\text{O}_9$ fabricated by rolling process. *J. Ceram. Soc. Jpn.* **117**(1365), 643–646 (2009)
 35. D. Segal, Chemical synthesis of ceramic materials. *J. Mater. Chem.* **7**(8), 1297–1305 (1997)
 36. B. Jaffe, *Piezoelectric Ceramics*. (Elsevier Science, 2012)
 37. P. Smaczyński, M. Sopicka-Lizer, K. Kozłowska, J. Plewa, Low temperature synthesis of calcium cobaltites in a solid state reaction. *J. Electroceram.* **18**(3), 255–260 (2007)
 38. S. Yu, S. He, H. Chen, L. Guo, Effect of calcination temperature on oxidation state of cobalt in calcium cobaltite and relevant performance as intermediate-temperature solid oxide fuel cell cathodes. *J. Power Sources* **280**, 581–587 (2015)
 39. F. Delorme, D. Ovono Ovono, P. Marudhachalam, C. Fernandez Martin, O. Fraboulet, Effect of precursors size on the thermoelectric properties of $\text{Ca}_3\text{Co}_4\text{O}_9$ ceramics. *Mater. Res. Bull.* **47**(5), 1169–1175 (2012)
 40. M. Presečnik, S. Bernik, Influence of a mechano-chemical treatment on the synthesis and characteristics of p-type thermoelectric $\text{Ca}_3\text{Co}_4\text{O}_9$ ceramics. *J. Alloys Compd.* **686**, 708–716 (2016)
 41. J. Antony, *Design of Experiments for Engineers and Scientists* (Elsevier Science, London, 2014)
 42. M. Campari, S. Garribba, The behavior of type K thermocouples in temperature measurement: The Chromel P-Alumel thermocouples. *Rev. Sci. Instrum.* **42**(5), 644–653 (1971)
 43. A.C. Masset, C. Michel, A. Maignan, M. Hervieu, O. Toulemonde, F. Studer, B. Raveau, J. Hejtmanek, Misfit-layered cobaltite with an anisotropic giant magnetoresistance: $\text{Ca}_3\text{Co}_4\text{O}_9$. *Phys. Rev. B* **62**(1), 166–175 (2000)
 44. P. Gerthsen, K.H. Härdtl, A. Csillag, Mobility determinations from weight measurements in solid solutions of $(\text{Ba}, \text{Sr})\text{TiO}_3$. *Phys. Status Solidi* **13**(1), 127–133 (1972)
 45. A.J. Moulson, J.M. Herbert, *Electroceramics* (Wiley, Chichester, 2003), p. 25
 46. A. Sotelo, F.M. Costa, N.M. Ferreira, A. Kovalevsky, M.C. Ferro, V.S. Amaral, J.S. Amaral, S. Rasekh, M.A. Torres, M.A. Madre, J.C. Diez, Tailoring $\text{Ca}_3\text{Co}_4\text{O}_9$ microstructure and performances using a transient liquid phase sintering additive. *J. Eur. Ceram. Soc.* **36**(4), 1025–1032 (2016)
 47. M.A. Madre, F.M. Costa, N.M. Ferreira, A. Sotelo, M.A. Torres, G. Constantinescu, S. Rasekh, J.C. Diez, Preparation of high-performance $\text{Ca}_3\text{Co}_4\text{O}_9$ thermoelectric ceramics produced by a new two-step method. *J. Eur. Ceram. Soc.* **33**(10), 1747–1754 (2013)
 48. W.D. Kingery, H.K. Bowen, D.R. Uhlmann, *Introduction to Ceramics* (Wiley, New York, 1976), pp. 449–452
 49. D.R. Lide, *CRC Handbook of Chemistry and Physics* (CRC Press, Boca Raton, 2003), pp. 744–750
 50. J. Hedvall, *Solid State Chemistry* (Elsevier, Amsterdam, 1966)
 51. H. Salmang, R. Telle, H. Scholze, *Keramik* (Springer, Berlin, 2006), pp. 376–377